Published in partnership with the Shanghai Institute of Ceramics of the Chinese Academy of Sciences



https://doi.org/10.1038/s41524-025-01665-8

Defect inducing large spin orbital coupling enhances magnetic recovery dynamics in Crl₃ monolayer

Check for updates

Yu Zhou¹, Ke Zhao¹⊠, Zhenfa Zheng², Huiwen Xiang¹, Jin Zhao²⊠ & Chengyan Liu¹⊠

The rapid magnetic recovery process (MRP) after photoexcitation is crucial for efficient information recording in magnets but is often impeded by insufficient spin flip channels. Using time-domain ab initio nonadiabatic molecular dynamics including spin-orbital coupling (SOC), we investigate MRP in a Crl_3 ferromagnetic monolayer and find that defects can accelerate this process. In defect-free Crl_3 , MRP is slow (400 fs) due to weak SOC between spin-majority and spin-minority valence band edges, notably limiting spin flips during relaxation. Intrinsic vacancy defects (V_1 and V_{Cr}), particularly the V_{Cr} defect, disrupt the system's rotational symmetry by extending their states asymmetrically to bulk I ions. The lowered symmetry significantly enhances SOC near the valence band edges and speeds up MRP to 100 fs by promoting spin flips. This study uncovers the origins of slow MRP in Crl_3 monolayer and highlights defect engineering as a promising strategy to improve MRP for optically excited spintronic devices.

Manipulating spin structures in matter using laser pulses has attracted extensive attention for its fast response, no need for external field and low power consumption¹⁻⁹. Specifically, applying this technique to emerging two-dimensional (2D) magnets, such as CrI₃, CrGeTe₂, MnS₂ and RuCl₃, could revolutionize future advancements in magnetic memory, data storage and spintronic devices^{1,10-19}. Experiments have observed that lasers can induce topological spin switching in CrGeTe2 van der Waals (vdW) magnets²⁰ and achieve all-optical magnetization switching in atomically thin CrI₃²¹. Theoretical studies indicate that laser pulses can drive transitions from antiferromagnet and ferrimagnet to transient ferromagnetic states in 2D Cr₂CCl₂/MnS₂ vdW heterostructure²² and 2D MXenes²³, respectively, and a transition from insulator to metal in layered α -RuCl₃²⁴. Although these studies demonstrate an ultrafast response of 2D magnets to light within tens of femtoseconds, the magnetic recovery process (MRP) after laser removal is relatively slow, typically occurring on a picosecond or sub-picosecond timescale^{3,7,12,13}. This slow MRP significantly limits the speed of information re-storage and re-recording in magnets. Therefore, understanding the physical mechanisms behind the slow MRP and exploring effective strategies are crucial for the design of advanced optical storage devices.

Ab initio nonadiabatic molecular dynamics (NAMD) including spin-orbital coupling (SOC) provides a powerful tool to understand SOC-induced spin dynamics in various materials^{22,23,25–28}. Recent studies reveal that electron-phonon coupling (EPC) facilitates direct

relaxation within same-spin states, while SOC induces spin flips between different spin states^{25,29,30}. As a relativistic effect, SOC is proportional to the fine structure constant and inversely proportional to the square of the speed of light, making it generally weaker than EPC effect³¹. This causes hot carriers to relax much more slowly when transitioning between different spin states compared to within same-spin states. MRP fundamentally involves spin flip of photoexcited electrons during relaxation, allowing them to return to their initial energy and spin states, making spin flips intrinsic to the process. Therefore, weak SOC effects between spin-majority (spin-up) and spin-minority (spin-down) states, which limit spin flip channels, likely account for the prolonged MRP after photoexcitation.

Previous studies have shown that structural defects can significantly lower crystalline symmetry in some semiconductors, leading to an enhanced SOC effect. This effect acts like an effective magnetic field, $B_{\rm eff} \propto [\nabla V(r) \times p]$, near defect site^{32,33}, where p and V(r) are momentum and crystal potential, respectively. For instance, theoretical calculations of Te-5p orbital-related defects in CdTe show large SOC effects, suggesting a need to reevaluate carrier nonradiative recombination centers in studies that previously omitted SOC considerations³⁴. Experiments have also demonstrated that $V_{\rm Se}$ and $V_{\rm S}$ defects in PtSe₂³⁵ and WS₂³⁶ monolayers, respectively, can cause large spin-orbital splitting of defect states in deep gaps, offering potential for spintronic device design. Therefore, inducing strong SOC effect

through defect engineering could be a promising strategy to accelerate MRP by opening additional spin flip channels in 2D magnets.

This work studies the SOC effects, enhanced by vacancy defects, on MRP after photoexcitation in a CrI $_3$ ferromagnetic monolayer using time-domain ab initio NAMD. Electronic structure analysis indicates that partial charge densities from both I and Cr vacancies ($V_{\rm I}$ and $V_{\rm Cr}$) extend to bulk I ions in an asymmetrical pattern. This lowered crystalline symmetry induces large SOC effects near the defect sites, opening more spin flip channels between spin-up and spin-down states near the valance band (VB) edges, thereby promoting the MRP. Multielectron NAMD simulations reveal that MRP in defective systems is several times faster than in pristine CrI $_3$ system, with recovery times ordered as $V_{\rm Cr}$ (~100 fs) < V $_{\rm I}$ (~200 fs) < pristine (~400 fs). The present work demonstrates that defect engineering offers a promising strategy for achieving rapid MRP after photoexcitation in 2D magnets.

Results and discussion Atomic and electronic structures of Crl₃ monolayer

Investigating the electronic structures of both defective and pristine CrI_3 systems is essential for understanding the SOC effects induced by defects on magnetic recovery dynamics (see electronic structure calculation in method section). The band structure in Fig. 1b shows that a pristine CrI_3 monolayer (primitive cell in the quadrilateral frame of Fig. 1a) is an intrinsic ferromagnetic semiconductor, with the valence band maximum (VBM) exhibiting higher spin-up (up-VB) than spin-down (dn-VB) states. In the V_I defect system, two spin-up defect levels (up-D) appear within the band gap, which are absent in the pristine system, as shown in Fig. 1d. Partial charge density of the V_I defect states on atomic structure is primarily concentrated on Cr ions adjacent to the V_I defect and I ions bonded to these Cr ions, as shown in Fig. 1c. The V_I defect states extend to bulk I ions, evident from the considerable weight of the defect states in both the spin-up and spin-down

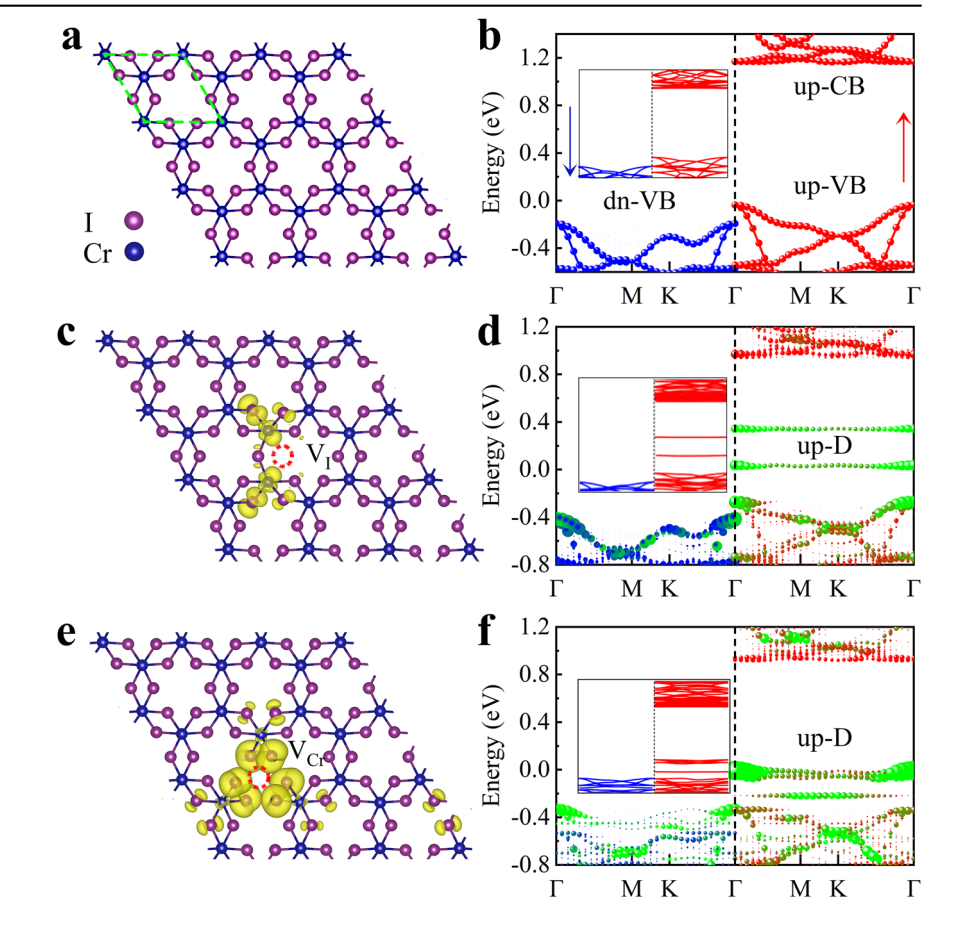
VBs (Fig. 1d), where I-5p orbitals mainly contribute to the VBs of CrI₃³⁷. The V_{Cr} defect, acting as an acceptor, introduces defect levels near the top of spin-up VB, as shown in Fig. 1f. It generates five defect levels, including two doublets (D1 and D2) and one singlet (D3) at the Γ-point, as detailed in Supplementary Fig. S1 (see Supplementary Information). Partial charge density indicates that the V_{Cr} defect states are primarily localized on the I ions originally bonded to the missing Cr and also extend to the next-nearest I ions in the bulk structure, as shown in Fig. 1e. Consequently, similar to the V_I defect system, both spin-up and spin-down VBs are partially influenced by the V_{Cr} defect states, as evidenced by the distribution of defect states in the energy bands shown in Fig. 1f. The partial charge densities of the V_I and V_{Cr} defect states, projected onto atomic structure, cause a notable reduction in rotational and translational symmetry of the systems, as shown in Fig. 1c, e. The lowered local symmetry could enhance SOC effects within the extended defect states^{32,33}, potentially opening spin flip channels between spin-up and spin-down VBs, thereby facilitating MRP.

Single-electron spin relaxation dynamics

To understand the impact of defects on MRP, it is instructive to study single-electron spin relaxation dynamics (see calculation details in NAMD simulation section), which reveal how an electron's population evolves at the band edges under the influence of EPC and SOC. Our tests of the single-electron relaxation process in the pristine system indicate that spin relaxation is insensitive to the choice of the initial state near the spin-up CBM, as shown in Supplementary Fig. S3. Therefore, to avoid redundancy, the minimum up-CB and the maximum dn-VB are designated as the initial and final states of the spin relaxation pathway, respectively, with all intermediate energy bands remaining unoccupied throughout the process. The band structure characteristics allow for three primary spin relaxation pathways: from up-CB to up-VB (process ①); from up-VB to dn-VB (process ②); and directly from up-CB to dn-VB (process ③), as illustrated in the schematics of

Fig. 1 | Atomic and electronic structures of pristine and defective ${\rm CrI}_3$ monolayer systems.

a, c, e Show atomic structures of the pristine, V_I and V_{Cr} systems in $3 \times 3 \times 1$ CrI₃ supercells, respectively. Violet and blue balls represent I and Cr atoms, respectively. The quadrilateral framed by green dashed lines in (a) represents the primitive cell. b, d, f Show the effective band structures unfolded in the primitive cell of the pristine, V_I and V_{Cr} systems, respectively. The inserts represent the corresponding supercell band structures. Red up arrow and blue down arrow denote spin-up and spin-down states, respectively. Green balls in (d, f) reflect the weight of defect states. The partial charge densities of VI and V_{Cr} defects in real space are shown in (c, e), respectively. The isovalue of isosurface charge density is 0.002 e/Å3. The intrinsic bands are labeled as up-CB for the spin-up conduction band (CB), up-VB for the spin-up VB and dn-VB for the spin-down VB. Defect levels within the band gap of spin-up states are classified as up-D. The Fermi level is set to energy zero point.



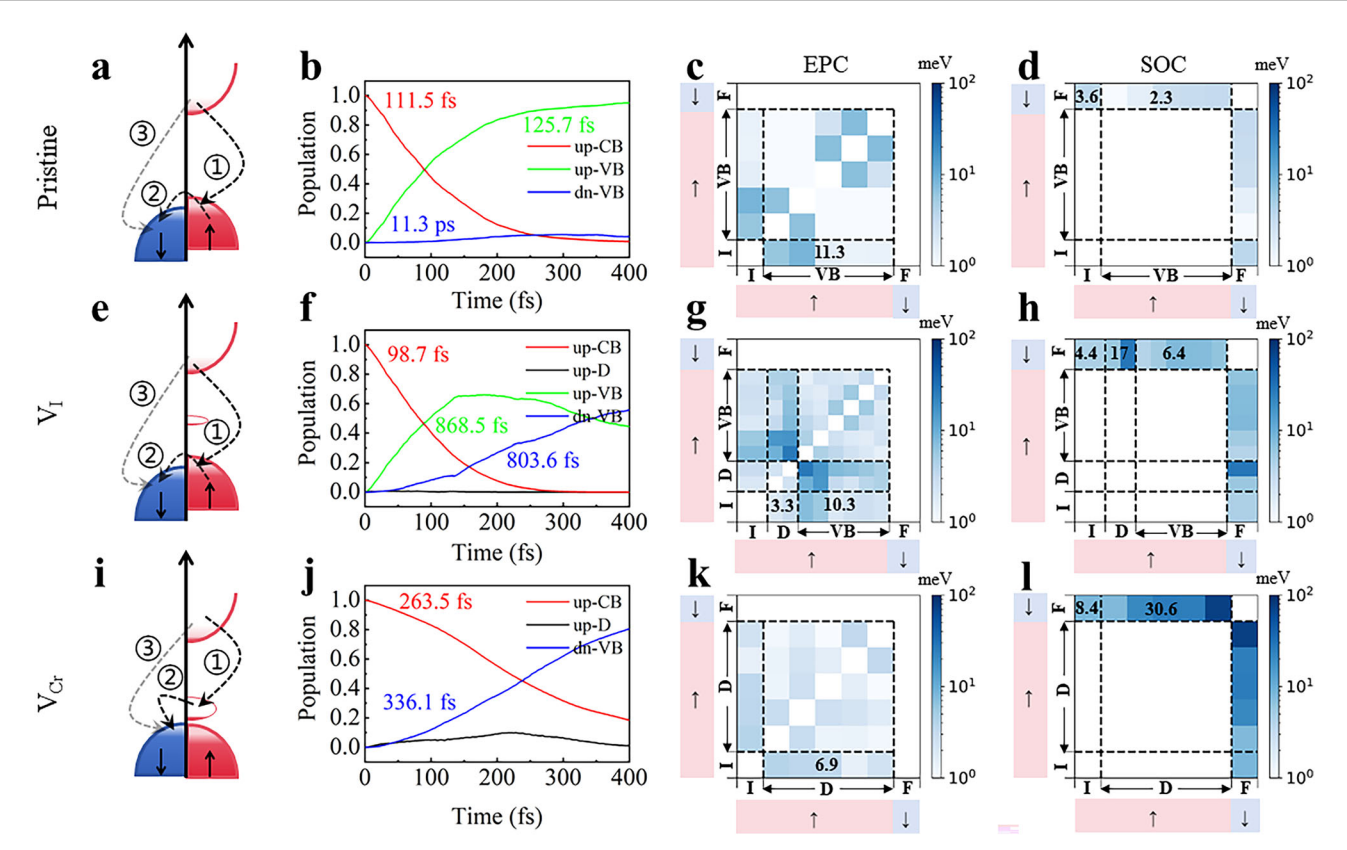


Fig. 2 | Single-electron spin relaxation dynamics in CrI_3 monolayers through NAMD simulations. a–d the pristine system, e–h the V_I defect system, and i–l the V_{Cr} defect system. a, e, i Schematic spin relaxation pathways, with black dashed arrows indicating possible electron transition. b, f, j Population evolution of electron in spin states, where the labels up-CB, up-VB, dn-VB and up-D in (b, f, j) are indicated in Fig. 1. c, g, k 2D visualization of EPC. d, h, l 2D visualization of SOC. Up arrow and down arrow denote spin-up and spin-down states, respectively. "I", "F"

and "D" represent initial, final and defect states, respectively. The spin lifetimes of excited electron in (**b**, **f**, **j**) are determined by fitting the population evolution curve with a Gaussian function. The initial and final states are the spin-up conduction band minimum (CBM) and spin-down VBM, respectively. The SOC between bands with same-spin states has a negligible effect on the spin flip process and is therefore not shown in the figures. Only SOC data with a significant impact on spin flip are presented. The complete SOC data are provided in Supplementary Fig. S2.

Fig. 2a (pristine) and 2e (V_I). In the V_{Cr} system, the dn-VB rises slightly above the up-VB (0.02 eV), leaving only the defect levels (up-D) within the active window. Hence, spin relaxation from up-D to dn-VB is designated as process @ in Fig. 2i.

In the pristine CrI₃ system, an electron in the minimum up-CB state rapidly relaxes to the up-VB via process ①, with a lifetime of 111.5 fs (Fig. 2b), as confirmed by the decrease in spin flux of the up-CB state (Supplementary Fig. S4 and see spin flux definition in part II of supplementary information). The electron then transitions from the up-VB to the maximum dn-VB much more slowly in process 2, with a lifetime of 11.3 ps (Fig. 2b). The reason is that, in process ①, electron transfers between two identical spin states (spin-up majority), dominated by EPC with a significant intensity of 11.3 meV (Fig. 2c). In processes 2 and 3, the SOC strengths between the initial and final states are only 2.3 and 3.6 meV (Fig. 2d), respectively, resulting in a very low transition probability for a spin-majority electron from the minimum up-CB to the spin-minority state in the maximum dn-VB. Therefore, in the pristine system, the spin-up electron primarily transfers energy to the lattice through EPC, preserving its spin state almost entirely. From a single-electron spin relaxation perspective, MRP of the pristine CrI₃ system involves a rapid transition of the photoexcited electron from CB to VB within spin-majority states but is impeded by spin relaxation between VBs in different spin states.

Defect states can induce significant SOC effects near defect sites by lowering crystalline symmetry potentially opening spin flip channels. In the V_I defect system, defect states (up-D) exist within the band gap between the up-CB and up-VB, as shown in Fig. 2e. In process \odot , electron lifetime in the minimum up-CB is 98.7 fs (Fig. 2f), slightly shorter than 111.5 fs in the pristine system. This reduction is attributed to the defect states providing

additional same-spin relaxing channels in the band gap (Fig. 2g). Moreover, defect states enable more channels (Fig. 2h) for spin flip between valence bands with different spin states, as shown in process \circledcirc of Fig. 2e. The electron population on the maximum dn-VB (Fig. 2f) increases significantly compared to the pristine case (Fig. 2b), indicating that the V_I defect accelerates MRP by promoting spin flips between the up-VB and the maximum dn-VB. Due to the small SOC of 4.4 meV between the minimum up-CB and maximum dn-VB in the V_I defect system (Fig. 2h), spin flips are unlikely in process \circledcirc , similar to the pristine system.

In the V_{Cr} system, the V_{Cr} defect reverses the original energy order of VBs, making the dn-VB slightly higher than the up-VB (Fig. 1f). The spin relaxation pathway begins at the minimum up-CB (up-CBM) and ends at the maximum dn-VB (up-VBM), with the possible pathways: from the up-CB to the up-D (process ①), from the up-D to the dn-VB (process ②), and directly from the up-CB to the dn-VB (process 3), as schematically shown in Fig. 2i. The relaxation time for an electron to transition from the up-CB to the up-D is 263.5 fs in process ① (Fig. 2j), notably longer than in the pristine (111.5 fs) and V_I defect (98.7 fs) systems. This prolonged relaxation time in the V_{Cr} system is due to the relatively small EPC between the up-CB and up-D states, only 6.9 meV, excluding the coupling between the up-CB and up-VB states (Fig. 2k). Due to the exceptionally large SOC of 30.6 meV between the dn-VB and up-D states (Fig. 21), electron relaxing from the up-CB to the up-D states rapidly migrates to the dn-VB states via spin flip, leaving almost no residual electron population in the up-D states, while significantly increasing the electron population in the dn-VB states (Fig. 2j). To clarify the impact of up-VBs, we conduct a comparative computational analysis of spin flip dynamics by designating the final state as a lower-energy dn-VB configuration containing two more intermediate upVB states (Supplementary Fig. S5a). Compared to the system without intermediate up-VB states (Supplementary Fig. S5b), the results exhibit an increase in spin flip rate when more up-VB states participate in the spin dynamics process. This enhancement can be attributed to the more SOC effects between different spin states, facilitated by the additional up-VB and dn-VB states, which act as intermediate channels to promote electron transitions from up-VB to dn-VB states.

To evaluate size effects, we further analyzed the spatial distribution of the $V_{\rm I}$ and $V_{\rm Cr}$ defect states (Supplementary Fig. S6) and the single-electron spin relaxation dynamics (Supplementary Fig. S7a, S7b) in a larger $4\times4\times1$ supercell, comparing them with results from the $3\times3\times1$ supercell (Figures S7c and S7d). The spatial distributions of defect states for the $V_{\rm I}$ and $V_{\rm Cr}$ defects in the $4\times4\times1$ supercell closely resemble these in the $3\times3\times1$ supercell. Moreover, in both supercells, the defects accelerate spin flip rate, and the evolution of electron spin follows a consistent trend. These findings confirm that the $3\times3\times1$ supercell is well-suited for simulating the MRP. Additionally, we have presented the evolution of Kohn-Sham orbitals (Supplementary Fig. S8), EPC (Supplementary Fig. S9) and SOC (Supplementary Fig. S10), all of which exhibit similar trends in both supercells.

Overall, vacancy defects ($V_{\rm I}$ and $V_{\rm Cr}$) in the CrI_3 monolayer induce substantial SOC effect between the top of the up-VB (up-D) and dn-VB states, thereby facilitating spin flip and accelerating the MRP. Further analyses of energy evolution and spin population also support these results (Supplementary Fig. S11). Nevertheless, it should be noted that the present framework does not account for the contributions from magnetic disorder and electron-electron scattering effects, both of which accelerate demagnetization demonstrated in Ni system³⁸. In addition, we compared the spin relaxation processes of hole and electron in the pristine and V_I systems (Supplementary Fig. S12), where intermediate up-VBs are involved in the relaxation pathways. The results show that in both systems, the relaxation rate of hole from dn-VB to up-CB is relatively faster than that of electron from up-CB to dn-VB. The reason is that when an electron relaxes from up-VBM to dn-VBM (Supplementary Fig. S13a), it primarily undergoes the spin-conserving process 2, which exhibits a much stronger EPC effect compared to the SOC-driven spin flip process ①. After entering the lower-energy up-VB via process ②, the electron undergoes a spin flip to dn-VB through process 3. In contrast, a hole relaxes from dn-VBM either by flipping to up-VBM via process @ or by flipping to the lower-energy up-VB via process (Supplementary Fig. S13b), with both processes involving spin flip. Therefore, unlike electron relaxation, which typically follows a spin-conserving process before undergoing a spin flip, hole relaxation is always accompanied by spin flip processes. Given the exclusion of magnetic disorder, electron-electron scattering and hole relaxation effects, we therefore speculate that the calculated magnetic recovery rates in our models are likely to be underestimated.

Multielectron spin relaxation dynamics

The study of excited single-electron spin relaxation reveals that the vacancy defects (V_I and V_{Cr}) in a CrI₃ monolayer accelerate MRP (corresponding process @ in Fig. 2) by enhancing SOC effects between different spin states. To further validate the picture that defect-induced SOC improves MRP, multielectron spin dynamics are simulated. Before that, we examine the magnet variation by using a laser pulse to excite electrons of CrI₃ monolayer, implemented in the PWmat package using GPU^{39,40}. The field's polarization is along the x- and y-directions expressed by a linear function $V_{\text{ext}}(r) = (x - 0.5) + (y - 0.5)$, since the systems are two-dimensional in our simulations. The Hamiltonian is expressed as $H(t) = H_0 + V_{\text{ext}}(r) \cdot E(t)$, where $E(t) = E_0 \exp[-\frac{(t-t_0)^2}{2\sigma^2}] \sin(\omega t + \frac{\pi}{2})$. $E_0 = 4 \text{ V/Å}$ is the strength of electric field, $t_0 = 30 \text{ fs}$, $2\sigma = 25 \text{ fs}$ is the pulse width, and $\omega = 3.6$ rad/fs is angular frequency, corresponding to a photon energy of 2.37 eV, which falls within the blue light range. This setup excites the valence band electrons to the up-CBs rather than the spindown conduction bands (dn-CBs). Under 8 fs of laser irradiation, the relative magnetic moment M_t/M_0 can reach 1.35 (Supplementary Fig. S14a), driven by electrons in dn-VBs first flowing into up-VBs before being excited to up-CBs (Supplementary Fig. S14b).

We use the relative magnetic moment after photoexciation as the initial state for demagnetization simulations via NAMD. To analyze spin flips in spin population, an equal number of spin-up and spin-down electrons (3.5% of the valence electrons) are excited from the up-VB and dn-VB states to the up-CB states within 0.5 eV above the spin-up CBM, setting as the systems' initial status in these simulations, with relative magnetic moments (~1.35) similar to the laser pulse case. We then compare the spin fluxes in the up-CB, up-VB and dn-VB electron reservoirs for the pristine, V_I and V_{Cr} systems in Fig. 3. It can be seen that processes ①, ⑤, and ⑦, driven by EPC (Fig. a, e, i), involve electron relaxation from high to low energy with spin conservation. Processes ②, ③, ④, and ⑥ are spin flip processes, where processes ②, ③, and ⑥ lead to a decrease in magnetic moment, while process ④ results in an increase, all governed by SOC (Fig. 3b, f, j).

Here, we primarily focus on the spin flip processes in magnetic recovery dynamics. In process ② of these three systems, the electron flow rate from up-CB to dn-VB is largest in the first few tens of femtoseconds, corresponding to the rapid decrease in magnetic moment, and then flattens out over the next few hundred femtoseconds (Fig. 3b, d, f, h, j, l). This corresponds to the rapid filling of the dn-VB, with the rate slowing as it approaches fullness, due to the strong SOC between the up-CB and the deep energy of dn-VB and the weak SOC between the up-CB and the top of the dn-VB, as shown in Supplementary Fig. S15.

Processes ③ and ④ correspond to electrons flow from up-VB to dn-VB and its reverse, respectively. The former reduces the relative magnetic moment, while the latter increases it. In both pristine and $V_{\rm I}$ systems, the flow rate of process ④ is larger than that of process ④, as their up-VB energies are higher than dn-VB energies (Fig. 3c, d, g, h). Therefore, the overall effect of these two processes is a reduction in the relative magnetic moment. In $V_{\rm Cr}$ system, process ④ is significantly enhanced due to the elevated dn-VB, which also increases the flow rate of process ②, where electrons flow from up-CB to dn-VB and then into up-VB through process ④ (Fig. 3j–l). Process ⑥ of defect systems reduces the relative magnetic moment, similar to process ③.

Overall, during the first few tens of femtoseconds, process @ dominates, with a large number of electrons transitioning from spin-up to spindown states, resulting in a rapid decay of the relative magnetic moment. As the VBs near full occupancy, the rate of process @ decreases rapidly, while processes 3, 4 and 6 take over, leading to a slow MRP. Therefore, the spin flip between up-VB and dn-VB ultimately determines the magnetic recovery rate. By analyzing the vibrational spectra of the maximum valence band and the chemical bonds near the V_I and V_{Cr} defect during ab initio molecular dynamics (AIMD) trajectories, we identified the primary phonon modes contributing to spin relaxation in valence bands as the vibration of two I atoms relative to the Cr atom near the vacancy defects (Supplementary Fig. S16). Compared to the pristine and V_I systems, the V_{Cr} system exhibits a significantly increased SOC (Supplementary Fig. S15a-5c) between the top regions of spin-up and spin-down VBs. This originates from the more diffusion of defect states on bulk I ions in the V_{Cr} system (Fig. 1e), leading to the fastest MRP in these three systems.

To visually present the MRP, the changes in the relative magnetic moment M_t/M_0 over time are investigated, as shown in Fig. 4. M_0 is the magnetic moment at the time of laser removal, while M_t is the magnetic moment at time t after laser removal. The initial M_t/M_0 is about 1.35, as we intentionally excite 3.5% of valence electrons from the up-VB and dn-VB states to the up-CB states. The magnetic moments of the pristine, $V_{\rm I}$ and $V_{\rm Cr}$ systems rapidly recover to 78%, 86% and 80% within the first 40 fs, and further to 89%, 97% and equilibrium at 100 fs, respectively. Finally, the pristine and V_I systems undergo a long MRP to reach convergence at 400 fs and 200 fs, respectively. These results indicate that the spin flip rate is faster during the initial relaxation stage than in the subsequent MRP, and vacancy defects, especially the V_{Cr} defect, significantly accelerate the MRP. Since photoexcitation-induced electrons transition from valence bands to conduction bands is a highly non-equilibrium process evidenced from the fluctuation curve in Supplementary Fig. S14b, different proportions of spin electrons in up-VB and dn-VB excited to up-CB with the same relative

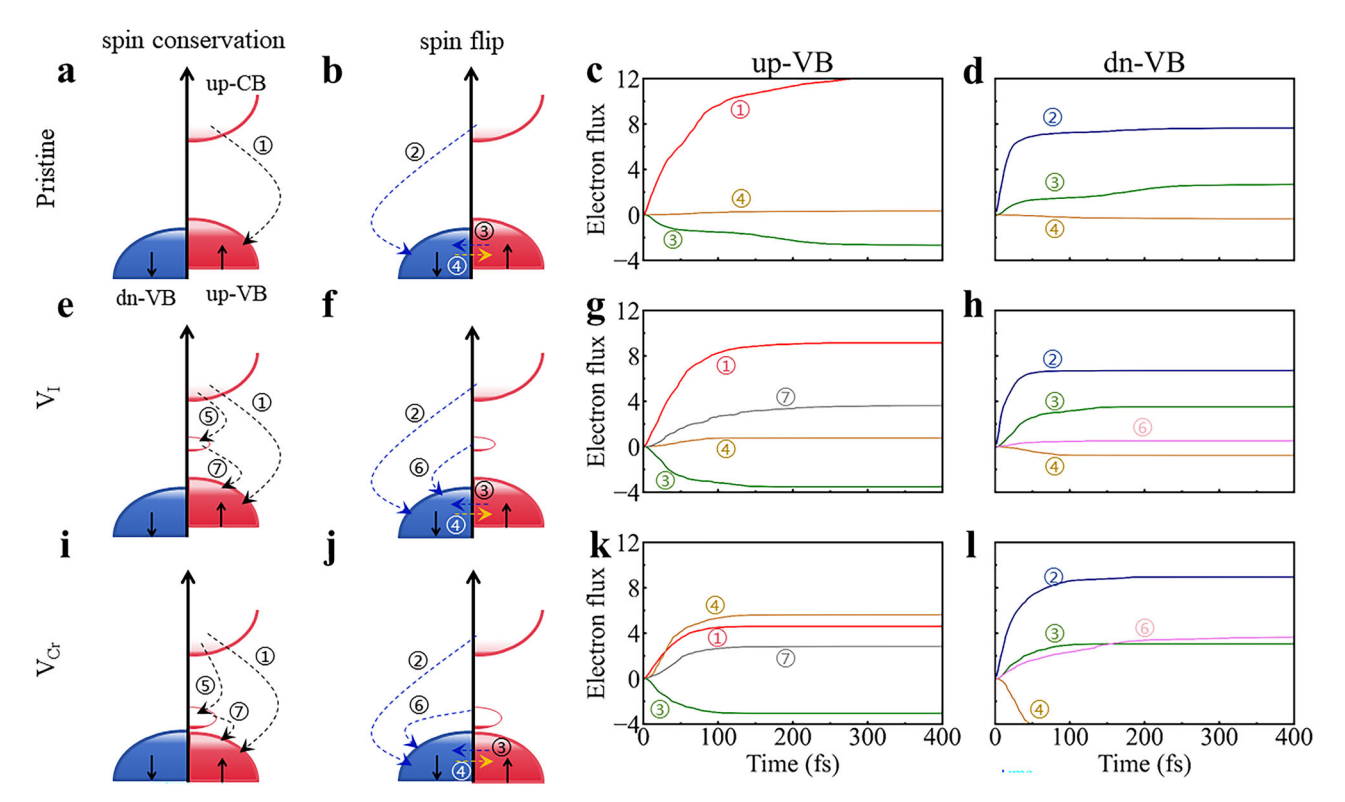


Fig. 3 | Relaxation pathways of multielectron spin dynamics and evoluation of electron flux. \mathbf{a} - \mathbf{d} the pristine system, \mathbf{e} - \mathbf{h} the V_I system and \mathbf{i} - \mathbf{l} the V_{Cr} system. \mathbf{a} , \mathbf{e} , \mathbf{i} Schematics of multielectron spin relaxation pathways with spin conversation. \mathbf{b} , \mathbf{f} , \mathbf{j} Schematics of multielectron spin relaxation pathways with spin flip. The blue dashed arrow represents the path of decreasing magnetic moment, while the orange dashed arrow represents the path of increasing magnetic moment. \mathbf{c} , \mathbf{g} , \mathbf{k} Evolution

of electron flux of the up-VB reservoir. **d**, **h**, **l** Evolution of electron flux of the dn-VB reservoir, also detailing both inflow and outflow pathways. Processes ① to ② correspond to specific spin relaxation pathways: process ②, up-CB to up-VB; process ②, up-CB to dn-VB; process ③, up-VB to dn-VB; process ③, dn-VB to up-VB; process ③, up-CB to up-D; process ⑥, up-D to dn-VB; and process ②, up-D to up-VB. The entire relaxation electron flux data is shown in Supplementary Fig. S17.

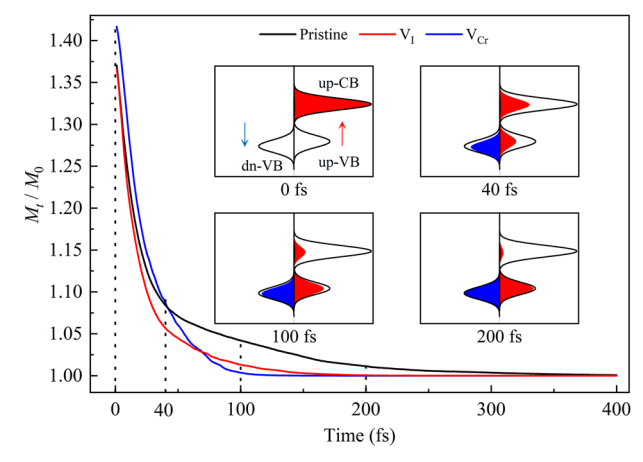


Fig. 4 | Evolution of relative magnetic moments for the pristine, V_I and V_{Cr} systems. Snapshots show the evolution of the occupied electron density of states in the pristine system from multielectron NAMD simulations. Black solid outlines represent the density of states. The filled red and blue areas indicate the occupation of spin-up and spin-down electronic states, respectively.

magnetic moment as the initial conditions in the pristine and $V_{\rm I}$ systems are examined for MRP as shown in Supplementary Fig. S18. The results show that defects accelerate magnetic recovery remains unaltered.

Taking the pristine CrI_3 system as a representative, the snapshots in Fig. 4 clearly show the evolution of the occupied electron density of states over time. At 0 fs, 3.5% valence electrons, equally distributing in the up-VB and dn-VB states, are excited to the up-CB states, leaving the corresponding up-VB and dn-VB states as empty electron reservoirs. By the first 40 fs, more

than half of these electrons have relaxed back to the up-VB and dn-VB states. This relaxation process is further enhanced by 100 fs, with only a few electrons remaining in the up-CB by 200 fs. Additionally, we examine a scenario where electrons excited to the up-CB states originate only from the up-VB states as the initial status for these three systems (Supplementary Fig. S19), which can be realized by polarized light^{41,42}. The results are consistent with those where electrons excited to the up-CB come equally from both the up-VB and dn-VB states (Fig. 4).

In this work, we utilize ab initio NAMD simulations including SOC to study spin relaxation dynamics in CrI $_3$ ferromagnetic monolayer. We find that in the pristine CrI $_3$ system, the prolonged MRP is due to the difficulty of spin flip near the upper regions of the spin-up and spin-down VBs, caused by their weak SOC. Introducing intrinsic vacancy defects (V $_{\rm I}$ and V $_{\rm Cr}$) significantly enhances the SOC effect between the band edges of VBs with different spin states, thereby accelerating MRP by facilitating spin flip. The underlying physical mechanism is that the electron density distribution from defect states, particularly the V $_{\rm Cr}$ defect, lowers the crystalline symmetry and extends significantly to bulk I ions, affecting the upper regions of the VBs. This study presents that vacancy defects enhance magnetic recovery dynamics in CrI $_{\rm 3}$ magnetic monolayer and highlights that defect engineering is a promising strategy to facilitate MRP, thereby advancing the development of optically controlled spintronic devices.

Methods

Electronic structure calculations

The electronic structures of both defect-free and defective systems are calculated based on a $3 \times 3 \times 1$ 2D supercell containing 18 Cr atoms and 54 I atoms. First-principles calculations are implemented with the Vienna ab initio simulation package 43,44 , employing the standard frozen-core projector-augmented-wave (PAW) method 45 . The Perdew-Burke-

Ernzerhof (PBE) functional with a spin polarization scheme is used for atomic relaxation 46 . To address the underestimation of the CrI band gap by the PAW method with PBE functional, a Hubbard U value of 3.0 eV is applied to the Cr-3d electrons, as referenced in previous theoretical studies 47,48 . The convergence criteria for Hellmann-Feynman forces and electronic energy are set to less than 0.01 eV/Å and 1 × 10 eV, respectively. An energy cutoff of 400 eV is used, and k points are sampled with a Γ-centered 2 × 2 × 1 mesh for Brillouin zone integration 49 . We map the energy eigenvalues obtained from large supercell calculations into an effective band structure (EBS) and recovers an approximate $E(\mathbf{k})^{50}$.

NAMD simulations

Ab initio molecular dynamics (AIMD) simulations are conducted using a single Γ -point with a 1 × 1 × 1 k-point mesh. Starting from fully relaxed models, the velocity rescaling method is employed to raise the system temperature up to 40 K (below Curie temperature¹¹) and maintain equilibrium for 2 ps under the canonical ensemble. Based on tests with 1 ps, 2 ps and 3 ps (Supplementary Fig. S20), 2 ps is sufficient to capture the effective phonon modes involved in the MRP. Subsequently, atomic trajectories are generated by AIMD for 2 ps in the microcanonical ensemble with a time step of 1.0 fs. The Kohn-Sham orbitals of the atomic trajectories are then used to calculate the nonadiabatic couplings in spindiabatic representation⁵¹. SOC effects are treated as a perturbation in this representation²⁵. Finally, NAMD simulations are performed to model spin electron transitions between defined initial and final states using the Hefei-NAMD software (see Nonadiabatic Molecular Dynamics Theory in part I of supplementary information), averaging 100 different AIMD atomic trajectories²⁵. In the process of simulating photo-excitation in PWmat, we also used PBE functional to relax the atomic structure. We added 3 eV of Hubbard *U* to the 3 d orbitals of Cr in TDDFT simulation using a single Γ -point with a $1 \times 1 \times 1$ k-point mesh. The relaxed structure was also heated to 40 K using velocity scaling method, and then laser was added for TDDFT simulation.

Data availability

The data supporting the findings of this study are available within the paper and its supplementary information file.

Code availability

The code for Hefei-NAMD-SOC, along with detailed instructions, is available at https://github.com/ZhenfaZheng/NAMDwithSOC.

Received: 20 December 2024; Accepted: 21 May 2025; Published online: 07 June 2025

References

- Sierra, J. F., Fabian, J., Kawakami, R. K., Roche, S. & Valenzuela, S. O. Van der Waals heterostructures for spintronics and opto-spintronics. Nat. Nanotechnol. 16, 856 (2021).
- Stamm, C. et al. Femtosecond modification of electron localization and transfer of angular momentum in nickel. *Nat. Mater.* 6, 740 (2007).
- Rudolf, D. et al. Ultrafast magnetization enhancement in metallic multilayers driven by superdiffusive spin current. *Nat. Commun.* 3, 1037 (2012).
- 4. Dabrowski, M. et al. Transition metal synthetic ferrimagnets: Tunable media for all-optical switching driven by nanoscale spin current. *Nano Lett.* **21**, 9210 (2021).
- Yao, K. et al. All-optical switching on the nanometer scale excited and probed with femtosecond extreme ultraviolet pulses. *Nano Lett.* 22, 4452 (2022).
- Batignani, G. et al. Probing ultrafast photo-induced dynamics of the exchange energy in a Heisenberg antiferromagnet. *Nat. Photonics* 9, 506 (2015).

- Kimel, A. V. et al. Room-temperature ultrafast carrier and spin dynamics in GaAs probed by the photoinduced magneto-optical Kerr effect. *Phys. Rev. B* 62. R10610 (2000).
- 8. Wang, M. et al. Photo-induced enhancement of lattice fluctuations in metal-halide perovskites. *Nat. Commun.* **13**, 1019 (2022).
- Penfold, T., Johansson, J. & Eng, J. Towards understanding and controlling ultrafast dynamics in molecular photomagnets. *Coord. Chem. Rev.* 494, 215346 (2023).
- Gong, C. et al. Discovery of intrinsic ferromagnetism in twodimensional van der Waals crystals. Nature 546, 265 (2017).
- 11. Huang, B. et al. Layer-dependent ferromagnetism in a van der Waals crystal down to the monolayer limit. *Nature* **546**, 270 (2017).
- He, J., Li, S., Frauenheim, T. & Zhou, Z. Ultrafast laser pulse induced transient ferrimagnetic state and spin relaxation dynamics in twodimensional antiferromagnets. *Nano Lett.* 23, 8348 (2023).
- Kirilyuk, A., Kimel, A. V. & Rasing, T. Ultrafast optical manipulation of magnetic order. Rev. Mod. Phys. 82, 2731 (2010).
- Jungwirth, T., Marti, X., Wadley, P. & Wunderlich, J. Antiferromagnetic spintronics. Nat. Nanotechnol. 11, 231 (2016).
- Bhatti, S. et al. Spintronics based random access memory: a review. Mater. Today 20, 530 (2017).
- Remy, Q. et al. Energy efficient control of ultrafast spin current to induce single femtosecond pulse switching of a ferromagnet. Adv. Sci. 7, 2001996 (2020).
- Mi, M. et al. Two-dimensional magnetic materials for spintronic devices. *Mater. Today Nano* 24, 100408 (2023).
- Choudhuri, I., Bhauriyal, P. & Pathak, B. Recent advances in graphene-like 2D materials for spintronics applications. *Chem. Mater.* 31, 8260 (2019).
- 19. Dabrowski, M. et al. Ultrafast thermo-optical control of spins in a 2D van der Waals semiconductor. *Nat. Commun.* **16**, 2797 (2025).
- Khela, M. et al. Laser-induced topological spin switching in a 2D van der Waals magnet. Nat. Commun. 14, 1378 (2023).
- 21. Zhang, P. et al. All-optical switching of magnetization in atomically thin Crl₃. *Nat. Mater.* **21**, 1373 (2022).
- Li, S., Zhou, L., Frauenheim, T. & He, J. Light-controlled ultrafast magnetic state transition in antiferromagnetic-ferromagnetic van der Waals heterostructures. *J. Phys. Chem. Lett.* 13, 6223 (2022).
- 23. He, J. & Frauenheim, T. Optically driven ultrafast magnetic order transitions in two-dimensional ferrimagnetic MXenes. *J. Phys. Chem. Lett.* **11**, 6219 (2020).
- Zhang, J. et al. Ultrafast spin dynamics and photoinduced insulatorto-metal transition in α-RuCl₃. Nano Lett. 23, 8712 (2023).
- Zheng, Z., Zheng, Q. & Zhao, J. Spin-orbit coupling induced demagnetization in Ni: ab initio nonadiabatic molecular dynamics perspective. *Phys. Rev. B* **105**, 085142 (2022).
- Gao, Y., Jiang, X., Qiu, Z. & Zhao, J. Photoexcitation induced magnetic phase transition and spin dynamics in antiferromagnetic MnPS₃ monolayer. *Npj Comput. Mater.* 9, 107 (2023).
- Zhang, P. et al. Strongly anisotropic ultrafast dynamic behavior of GaTe dominated by the tilted and flat bands. *Nanotechnology* 34, 285703 (2023).
- Ghosh, A., Kumar, S. & Sarkar, P. Point defect-mediated hot carrier relaxation dynamics of lead-free FASnl₃ perovskites. *Nanoscale* 16, 4737 (2024).
- Lu, H. & Long, R. Ab initio nonadiabatic molecular dynamics of ultrafast demagnetization in iron. *J. Phys. Chem. Lett.* 14, 5403 (2023).
- 30. Lu, H., Long, R. & Fang, W.-H. Electron-versus spin-phonon coupling governs the temperature-dependent carrier dynamics in the topological insulator Bi₂Te₃. *J. Am. Chem. Soc.* **145**, 25887 (2023)
- Bychkov, Y. A. & Rashba, E. I. Oscillatory effects and the magnetic susceptibility of carriers in inversion layers. *J. Phys. C: Solid State Phys.* 39, 66 (1984).

- Rashba, E. I. Properties of semiconductors with an extremum loop. 1.
 Cyclotron and combinational resonance in a magnetic field perpendicular to the plane of the loop. Sov. Phys. Solid State 2, 1109 (1960).
- 33. Dresselhaus, G. Spin-orbit coupling effects in Zinc blende structures. *Phys. Rev.* **100**, 580 (1955).
- Pan, J., Metzger, W. K. & Lany, S. Spin-orbit coupling effects on predicting defect properties with hybrid functionals: A case study in CdTe. *Phys. Rev. B* 98, 054108 (2018).
- Absor, M. A. U. et al. Defect-induced large spin-orbit splitting in monolayer PtSe₂. Phys. Rev. B 96, 115128 (2017).
- Schuler, B. et al. Large spin-orbit splitting of deep in-gap defect states of engineered sulfur vacancies in monolayer WS₂. Phys. Rev. Lett. 123, 076801 (2019).
- Mukherjee, T., Chowdhury, S., Jana, D. & Voon, L. C. L. Y. Strain induced electronic and magnetic properties of 2D magnet Crl₃: a DFT approach. *J. Phys.: Condens. Matter* 31, 335802 (2019).
- Chen, Z. & Wang, L.-W. Role of initial magnetic disorder: a timedependent ab initio study of ultrafast demagnetization mechanisms. Sci. Adv. 5, eaau8000 (2019).
- 39. Jia, W. et al. The analysis of a plane wave pseudopotential density functional theory code on a GPU machine. *Comput. Phys. Commun.* **184**, 9 (2013).
- Wang, Z., Li, S.-S. & Wang, W.-L. Efficient real-time timedependent density functional theory method and its application to a collision of an ion with a 2D material. *Phys. Rev. Lett.* 114, 063004 (2015).
- Zeng, H., Dai, J., Yao, W., Xiao, D. & Cui, X. Valley polarization in MoS₂ monolayers by optical pumping. *Nat. Nanotechnol.* 7, 490 (2012).
- 42. Rong, R. et al. The interaction of 2D materials with circularly polarized light. *Adv. Sci.* **10**, e2206191 (2023).
- Kresse, G. & Furthmüller, J. Efficiency of ab-initio total energy calculations for metals and semiconductors using a plane-wave basis set. Comput. Mater. Sci. 6, 15 (1996).
- Kresse, G. & Furthmüller, J. Efficient iterative schemes for ab initio total-energy calculations using a plane-wave basis set. *Phys. Rev. B* 54, 11169 (1996).
- Kresse, G. & Joubert, D. From ultrasoft pseudopotentials to the projector augmented-wave method. *Phys. Rev. B* 59, 1758 (1999).
- Perdew, J. P., Burke, K. & Ernzerhof, M. Generalized gradient approximation made simple. *Phys. Rev. Lett.* 77, 3865 (1996).
- Sivadas, N., Okamoto, S., Xu, X., Fennie, C. J. & Xiao, D. Stackingdependent magnetism in bilayer Crl₃. Nano Lett. 18, 7658 (2018).
- Zhou, Z. et al. Ultrafast laser control of antiferromagneticferrimagnetic switching in two-dimensional ferromagnetic semiconductor heterostructures. Nano Lett. 23, 5688 (2023).
- Monkhorst, H. J. & Pack, J. D. Special points for Brillouin-zone integrations. *Phys. Rev. B* 13, 5188 (1976).
- Popescu, V. & Zunger, A. Extracting E versuseffective band structure from supercell calculations on alloys and impurities. Phys. Rev. B 85, 085201 (2012).

 Zheng, Q. et al. Ab initio nonadiabatic molecular dynamics investigations on the excited carriers in condensed matter systems. WIREs Comput. Mol. Sci. 9, e1411 (2019).

Acknowledgements

This research was sponsored by the Natural Science Foundation of Henan, Henan Province Outstanding Youth Science Foundation (Grants No. 252300421215); Key Scientific Research Project of Higher Education Institutions in Henan Province - Basic Research Program (Grants No. 25ZX005); National Natural Science Foundation of China (Grants No. 12274114).

Author contributions

J.Z. and C.Y.L. conceived this project and designed the studies. Y.Z., K.Z. and Z.Z. performed the calculation and analyzed the data. K.Z. and H.W.X. established the models and plotted all the figures. The main manuscript was written by C.Y.L., and J.Z. All authors reviewed the manuscript.

Competing interests

The authors declare no competing interests.

Additional information

Supplementary information The online version contains supplementary material available at https://doi.org/10.1038/s41524-025-01665-8.

Correspondence and requests for materials should be addressed to Ke Zhao, Jin Zhao or Chengyan Liu.

Reprints and permissions information is available at http://www.nature.com/reprints

Publisher's note Springer Nature remains neutral with regard to jurisdictional claims in published maps and institutional affiliations.

Open Access This article is licensed under a Creative Commons Attribution-NonCommercial-NoDerivatives 4.0 International License, which permits any non-commercial use, sharing, distribution and reproduction in any medium or format, as long as you give appropriate credit to the original author(s) and the source, provide a link to the Creative Commons licence, and indicate if you modified the licensed material. You do not have permission under this licence to share adapted material derived from this article or parts of it. The images or other third party material in this article are included in the article's Creative Commons licence, unless indicated otherwise in a credit line to the material. If material is not included in the article's Creative Commons licence and your intended use is not permitted by statutory regulation or exceeds the permitted use, you will need to obtain permission directly from the copyright holder. To view a copy of this licence, visit https://creativecommons.org/licenses/by-nc-nd/4.0/.

© The Author(s) 2025